Structural evolution of poly(butylene succinate) crystals on heating with the formation of a dual lamellar population, as monitored by temperature-dependent WAXS/SAXS analysis

Maria Cristina Righetti [a,*], Maria Laura Di Lorenzo [b], Dario Cavallo [c], Alejandro J. Müller [d,e], Massimo Gazzano [f]

[a] *CNR-IPCF, National Research Council – Institute for Chemical and Physical Processes, Via Moruzzi 1, 56124, Pisa, Italy*
[b] *CNR-IPCB, National Research Council – Institute of Polymers, Composites and Biomaterials, Via Campi Flegrei 34, 80078, Pozzuoli, Italy*
[c] *Department of Chemistry and Industrial Chemistry, University of Genoa, 16146, Genova, Italy*
[d] *POLYMAT and Department of Polymers and Advanced Materials: Physics, Chemistry and Technology, Faculty of Chemistry, University of the Basque Country UPV/ EHU, Paseo Manuel de Lardizabal 3, 20018, Donostia-San Sebastián, Spain*
[e] *IKERBASQUE, Basque Foundation for Science, Plaza Euskadi 5, 48009, Bilbao, Spain*
[f] *CNR-ISOF, National Research Council – Institute of Organic Synthesis and Photoreactivity, Via Gobetti 101, 40129, Bologna, Italy*

ARTICLE INFO

ABSTRACT

The structural evolution of poly(butylene succinate) (PBS) crystals after crystallization at 100 °C has been investigated by synchrotron wide-angle and small-angle X-ray scattering (WAXS and SAXS) analysis. Isothermal crystallization of PBS leads to a single lamellar population. Temperature-dependent WAXS/SAXS analysis has proven that an additional crystal population, characterized by thicker lamellae, develops upon heating, resulting in a dual lamellar population. Deconvolution of the Lorentz-corrected double SAXS profiles has allowed deriving the temperature dependence of the lamellar thickness for the two different crystal populations. The structural information derived by WAXS/SAXS has allowed elucidating the multiple melting behavior of PBS, so that the separate endotherms of the overall melting behavior could be associated with specific thermal events. The first melting peak has been connected to the fusion of original crystals, only minimally reorganized upon heating, whereas the second melting peak has been ascribed to the overlapping of two different melting processes, one linked to the fusion of original crystals thickened at high temperatures, most likely in the solid state, and the other one to the fusion of markedly thicker crystals, developed via melting/recrystallization mechanism.

1. Introduction

Poly(butylene succinate) (PBS) is a biobased and compostable linear polyester with remarkable thermal and mechanical properties [1–3]. Similar to widely used polyolefins, like isotactic polypropylene (iPP) or high-density and low-density polyethylene (HDPE and LDPE), PBS has a glass transition temperature (T_g) well below room temperature, around −30 °C, a relatively high melting temperature (above 100 °C), and a very high crystallization rate upon cooling from the isotropic melt [1–6]. Also, the mechanical properties of PBS do not differ substantially from those of iPP, HDPE, and LDPE [7]: PBS is a very ductile polymer, despite the fast degradation upon storage may cause a drop in ductility, turning PBS into a brittle polymer [8]. In addition, PBS is a "green" polymer because it is biodegradable, compostable, and can be produced from

renewable sources, like cellulose and starch-based biomass [9,10]. Moreover, PBS is also biocompatible, which enables biomedical applications [11], and it is approved for food contact, hence is used in food packaging [7,12], either plain, or blended with other "green" polymers, mainly poly(lactic acid), starch, polyhydroxyalkanoates, or proteins [2, 3,13].

For these reasons, in times of growing environmental awareness, PBS has been the topic of many investigations, with several studies devoted to a thorough investigation of its structure and properties. Thermal properties of PBS are particularly intriguing, as PBS displays some unique features, like the development of crystallinity at temperatures below T_g. In initially amorphous PBS, crystal formation at low temperatures was linked to complete densification of the glass, which allowed formation of homogeneous crystal nuclei and their growth [14]. Also the

---

partially crystallized PBS can further crystallize at temperatures below T_g, likely due to constrained amorphous segments coupled with the crystals that transform into ordered phase [15]. PBS also displays a very complex melting behavior, which, depending on crystallization temperature and heating rate, can display up to four melting endotherms [14–25].

Multiple endotherms in the melting range are not peculiar to PBS, but are often encountered upon heating several semi-crystalline polymers at the rates typical of differential scanning calorimetry (DSC), generally from 2 to 50 K/min. Multiple endotherms may originate from a number of different phenomena, like the presence of more than one crystalline form [26], or crystalline populations with different stability or morphology [27–29], molar mass segregation during crystallization or crystal perfection [30,31], fusion of confined nanocrystals [32], orientation effects [33], devitrification of rigid amorphous fraction (RAF) [34–36] or more often, partial melting followed by recrystallization and remelting [37,38]. However, regarding the possible influence of the rigid amorphous fraction, it was recently reported that RAF in PBS devitrifies at about 25 °C [23], well below the onset of crystal melting, which excludes any possible contribution of the RAF to the multiple melting of PBS.

For PBS, melt or cold crystallization in a wide temperature range leads to crystallization in a single crystal modification, named α-form [16,21,23], which has a monoclinic unit cell with lattice parameters $a = 0.523$ nm, $b = 0.908$ nm, $c = 1.080$ nm, and β = 123.9° [39,40]. PBS can also develop another crystal modification, called β-form, where the polymer chains are in *trans* conformation and packed in a monoclinic unit cell with lattice dimensions $a = 0.584$ nm, $b = 0.832$ nm, $c = 1.186$ nm, and β = 131.6° [40]. β-form is observed only upon stretching α-form crystals, with the peculiarity that the solid-state crystal transition is totally reversible [41].

To date, melting/recrystallization/remelting mechanism appears as the most accepted explanation of the PBS multiple melting behavior [15–25], although also the coexistence of melting/-recrystallization/remelting and two crystal populations with different thermal stability, both assumed originating during crystallization, has been hypothesized [16,21]. Actually, recent studies by fast scanning chip calorimetry (FSC) proved that a single crystal population develops in PBS during isothermal crystallization at high and low undercooling because only one melting peak was detected by heating the polymer at heating rates sufficiently high to suppress recrystallization [24,25]. Thus, if the PBS complex melting behavior at conventional heating rates is originated by a second crystalline population, the latter necessarily must develop not during crystallization but upon subsequent heating.

In the present study, the structural changes occurring upon heating in a PBS sample crystallized at 100 °C have been followed by synchrotron X-ray technique. Wide-angle and small-angle X-ray scattering (WAXS and SAXS) measurements have been performed upon heating in parallel with conventional DSC analysis to obtain structural details regarding the crystal lattice and the lamellar morphology and to correlate the structural evolution to the melting behavior. In a forthcoming paper the reorganization occurring after crystallization at different temperatures, perfectly in line with the results of this study, will be presented. A full understanding of the origin of the PBS multiple melting endotherm is expected to allow new insights into the crystallization process of this polymer and, in general, of semi-crystalline polymers.

2. Materials and methods

2.1. Materials

Additive-free poly(butylene succinate) (PBS) was kindly supplied by SIPOL (Mortara, Italy). Molar mass and molar mass distribution were measured by Gel Permeation Chromatography (GPC). The analysis was performed using a GPC Max Viscotek system equipped with a TDA 305 triple detector and Phenogel column set composed of a precolumn and two columns with exclusion limit respectively of 10^6 and 10^3 g/mol. All the samples were dissolved and eluted in chloroform stabilized with ethanol, and then filtered on PTFE 0.22 μm membranes. The injection volume was 100 μl, the flow rate 0.8 ml/min, and the sample concentrations were about 5 mg/ml. The measurements, performed at 35 °C according to the temperatures of columns and detectors, ran for 50 min in duplicate. Universal Calibration based on polystyrene standards $(2 \cdot 10^3 – 5.6 \cdot 10^5$ g/mol) was used. The number-average molar mass (M_n) and the weight-average molar mass (M_w) were $2.8 \cdot 10^4$ and $7.3 \cdot 10^4$ g/mol, respectively.

The as-received PBS chips were dried at 60 °C under vacuum overnight. Dried chips were used to prepare films with a thickness of about 200 μm by compression-molding with a Collin Hydraulic Laboratory Forming Press P 200 E at 130 °C for 3 min. Then the films were cooled to room temperature by cold water circulating into the press plates. GPC analyses revealed no significant change of PBS molar mass after compression-molding.

2.2. Thermal analysis by differential scanning calorimetry (DSC)

Thermal analysis was performed by means of a PerkinElmer Calorimeter DSC 8500, equipped with an IntraCooler III as refrigerating system. The instrument was calibrated in temperature with high purity standards (indium, naphthalene, cyclohexane) according to the procedure for standard DSC [42]. Enthalpy calibration was performed with indium. Dry nitrogen was used as purge gas at a rate of 20 mL/min. To gain precise heat capacity data from the heat flow rate measurements, each scan was accompanied by a blank run with an empty pan. The mass of the blank and sample aluminum pans matched within 0.02 mg. The temperature of the samples upon heating was corrected for the thermal lag, determined as average by using different standard materials. This lag was 0.05 min, which, for the heating rates of 2 K/min, corresponds to a temperature correction of −0.1 K.

Before each analysis, the PBS samples were heated in the DSC to 150 °C at 20 K/min and then maintained at this temperature for 3 min to erase the thermal history. Isothermal crystallization experiments in the temperature range $80 \leq T_c \leq 108$ °C were performed in the DSC after cooling (effective rate: 150 K/min) from 150 °C to T_c. The samples were crystallized for times sufficient to obtain the leveling of the heat flow rate signal after the exothermal peak (15 min at 80 °C, 20 min at 84 °C, 25 min at 88 °C, 50 min at 92 °C, 140 min at 96 °C, 5 h at 100 °C, 16 h at 104 °C, and 48 h at 108 °C). The melting behavior after complete isothermal crystallization was investigated by heating the PBS samples at 2 K/min directly from T_c, to obtain apparent specific heat capacity ($c_{p, app}$) curves.

2.3. Wide-angle and small-angle X-ray scattering (WAXS and SAXS) characterization

Simultaneous wide-angle and small-angle X-ray scattering (WAXS and SAXS) measurements were performed in transmission geometry using synchrotron radiation at beamline BM26 of the European Synchrotron Radiation Facility (ESRF), Grenoble, France. The sample was arranged in ambient atmosphere in such a way that the X-ray beam passed directly through the *in-line* differential scanning calorimetry LINKAM DSC 600. X-ray scans were collected each 0.5 K during the heating ramp at 2 K/min. The magnitude of the scattering vector q defined by $q = (4\pi/\lambda) \sin\theta$, where $\lambda = 0.10332$ nm (12 keV) is the wavelength of the X-ray source and 2θ the scattering angle, was calibrated using silver behenate. Patterns were recorded with Pilatus 1 M 2D (WAXS) and Pilatus 300K–W (SAXS) detectors. The X-ray analysis, including background subtraction and radial integrations of the 2D patterns, was performed using home-built routines of BUBBLE software package [43]. From the WAXS patterns, the unit cell parameters were calculated by a least squares fitting method through minimization of the
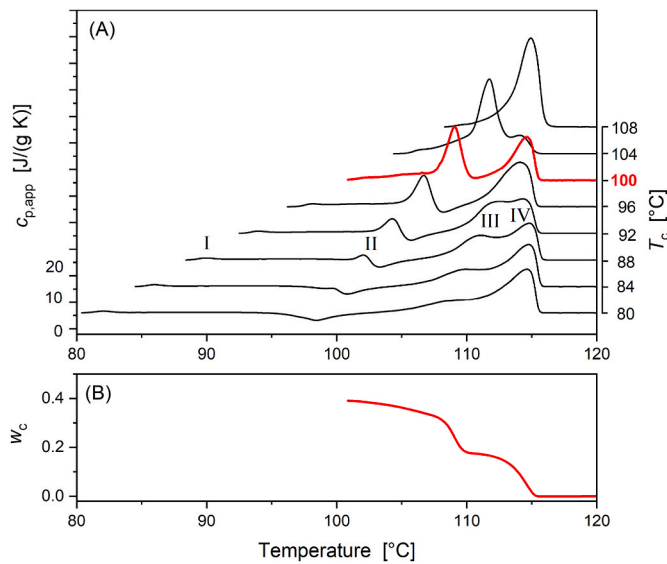
Fig. 1. (A) Apparent specific heat capacity ($c_{p,app}$) curves at 2 K/min after isothermal crystallization at the specified T_cs. The ordinate values refer only to the bottom curve. All the other curves are shifted vertically for the sake of clarity. The endothermic events are labeled I, II, III, and IV in order of increasing temperature; (B) Temperature evolution of the crystal weight fraction (w_c) after crystallization at $T_c = 100$ °C upon heating at 2 K/min, calculated from the relative $c_{p,app}$ curve. In both sections (A) and (B), the red color refers to $T_c = 100$ °C. (For interpretation of the references to color in this figure legend, the reader is referred to the Web version of this article.)

differences between measured and calculated position of the five most intense peaks.

The SAXS pattern recorded in the melt at 180 °C, originating from electron density fluctuation and scattering due to possible foreign particles and voids, was utilized as blank pattern and subtracted from all the SAXS profiles at the various temperatures. Then, after multiplication by q^2, the Lorentz-corrected SAXS intensities where obtained. The scattering invariant Q was determined from the Lorentz-corrected SAXS profiles from:

$$Q = \int_0^\infty I q^2 dq \tag{1}$$

being approximately defined as [44–46]:

$$Q = K \alpha_S x_{c,l} \left(1 - x_{c,l}\right) \left(\rho_c - \rho_a\right)^2 \tag{2}$$

where K is a constant, α_S is the volume fraction of the lamellar stacks within the total irradiated sample volume, $x_{c,l}$ is the linear crystallinity in the stack (with the product $\alpha_S x_{c,l}$ corresponding to the volumetric bulk crystallinity x_c), and ρ_c and ρ_a are the densities of the crystalline and amorphous fractions, which are proportional to the electron densities of the crystalline and amorphous layers, with the proportionality constant included in K, the constant that takes into account also the non-absolute scale of the SAXS intensities [47,48]. By Fourier transformation of the Lorentz-corrected SAXS intensities, the one-dimensional correlation functions $K(z)$, with z corresponding to the direction normal to the layers faces in the stack, were calculated [47–49]:

$$K(z) = \int_0^\infty I q^2 \cos(qz) dq \tag{3}$$

3. Results and discussion

### 3.1. Multiple melting behavior of PBS as a function of T_c

Fig. 1(A) displays the $c_{p,app}$ curves upon heating at 2 K/min, directly from T_c, after isothermal crystallization at $80 \leq T_c \leq 108$ °C. A low heating rate was chosen for a better resolution and a more confident comparison between DSC and WAXS/SAXS data. Similar multiple melting behavior was observed also at 10 and 20 K/min, which attests that the PBS reorganization is not a slow process [16,19–21]. Fig. 1(A) attests that the number of the melting endotherms depends on T_c. The endothermic events are labeled I, II, III, and IV in order of increasing temperature. The small peak observed at temperatures slightly above T_c, often called "annealing peak" (peak I), is common to many semi-crystalline polymers, and frequently associated either to RAF devitrification or to fusion of less perfect secondary crystals [34–36,50]. In the presence of a single crystalline population, as it is the case of PBS [24,25], it can be explained as due to the offset between initial melting and subsequent recrystallization [37,51]. The possibility that the first small peak can originate from structural relaxation connected to RAF devitrification has to be ruled out for PBS, as mentioned in the Introduction, because full devitrification of the RAF is attained at 25 °C. At higher temperatures, a second peak appears before an exothermic process that is well evident up to $T_c = 96$ °C. The second peak (peak II) shifts to higher temperatures with increasing T_c, and in parallel also its area increases so that it becomes predominant for $T_c \geq 104$ °C. A double or a single endotherm concludes the melting process, with the two final peaks (peaks III and IV) that progressively merge into a single one. In summary, in addition to the annealing peak, the melting behavior of PBS shown in Fig. 1 comprises: three endotherms after crystallization at $T_c \leq 92$ °C, two endotherms for $96 \leq T_c \leq 104$ °C, and one endotherm for $T_c = 108$ °C.

As a single crystalline population develops in PBS during isothermal crystallization [24,25], it is unquestionable that the different overall melting behaviors must correspond to different crystalline re-organizations. As an initial analysis, the present paper is focused on investigating the structural changes of the PBS crystal fraction upon heating after crystallization at $T_c = 100$ °C. The relative melting behavior, highlighted in red in Fig. 1(A), comprises, in addition to the annealing peak, two distinct endotherms centered at 109 and 114.5 °C.

The weight fraction crystallinity (w_c) of PBS crystallized at $T_c = 100$ °C, and its evolution upon heating at 2 K/min was calculated from the $c_{p,app}$ curve by Eq. (4) [52]:

$$w_c(T) = \int_T^{T_o} \frac{c_{p,app}(T') - c_{p,base}(T')}{\Delta h_m^\circ(T')} dT' \tag{4}$$

where T_o is a reference temperature in the melt, $\Delta h_m^\circ(T)$ is the temperature dependence of the enthalpy of melting of 100% crystalline PBS [$\Delta h_m^\circ(T) = 141 + 0.57\,T - 0.0008\,T^2$ J/g with T in °C] [23], and $c_{p,base}$ is the baseline specific heat capacity. For PBS, the upper temperature limit for the presence of the rigid amorphous fraction is 25 °C [23], hence above 25 °C $c_{p,base}$ can be described by a two-phase model by taking into account the crystal fraction (solid) and a single amorphous (liquid) fraction. As first approximation, $c_{p,base}$ was assumed linear from 100 °C to the end of melting and then progressively adjusted up to obtain constant $w_C(T)$, being $c_{p,base}(T) = w_C(T) c_{p,s}(T) + [1-w_C(T)] c_{p,l}(T)$ [52], with $c_{p,s}$ and $c_{p,l}$ corresponding to the thermodynamic specific heat capacities of the solid and liquid PBS ($c_{p,s}(T) = 1.22 + 0.0031\,T$ and $c_{p,l} = 179 + 0.0016\,T$ with $c_{p,s}$ and $c_{p,l}$ in J g^{-1} K^{-1} and T in °C) [23]. The calculated w_C curve is displayed in Fig. 1(B). The initial crystal weight fraction is 0.39. The crystallinity starts to decrease immediately upon heating, with a double step trend, in agreement with the two endotherms reported in Fig. 1(A).
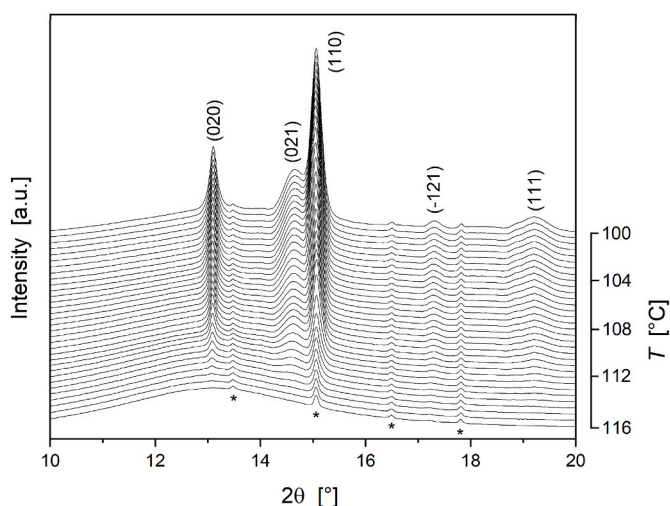
Fig. 2. Temperature-resolved WAXS profiles of PBS upon heating (heating rate: 2 K/min) after isothermal crystallization at $T_c = 100$ °C. The asterisks mark peaks due to the instrumental apparatus.
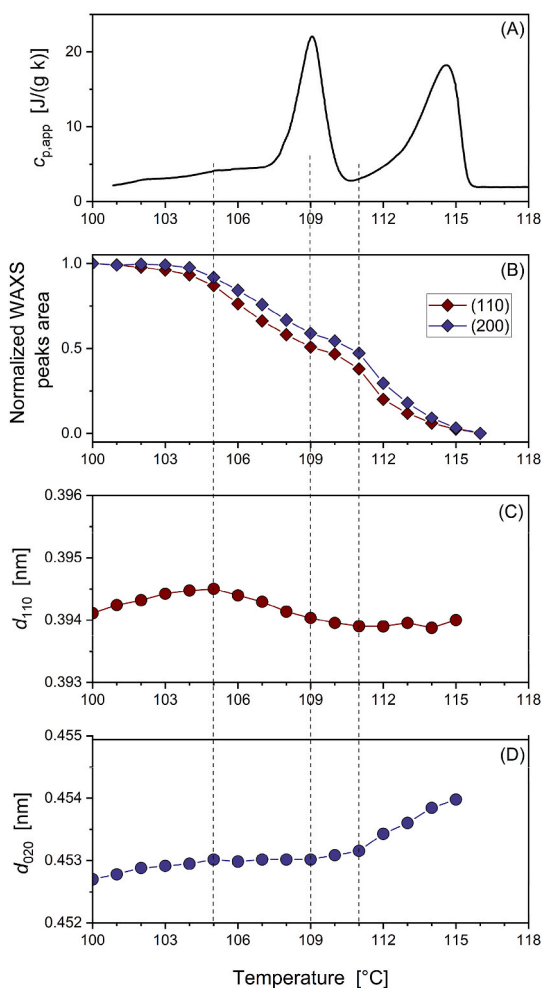
Fig. 3. (A) Apparent specific heat capacity ($c_{p,app}$) curve at 2 K/min after isothermal crystallization at $T_c = 100$ °C; (B) Normalized areas of the (110) and (020) reflections as a function of temperature; (C) Temperature evolution of the d_{110} spacing; (D) Temperature evolution of the d_{200} spacing. The vertical dashed lines mark the temperatures at which changes in the crystalline parameters are observed.
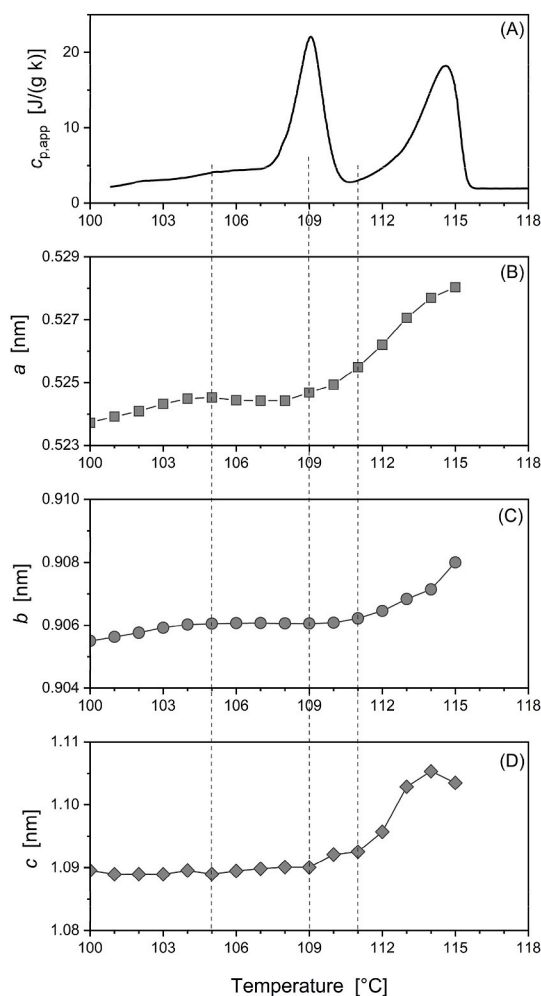
Fig. 4. (A) Apparent specific heat capacity ($c_{p,app}$) curve at 2 K/min after isothermal crystallization at $T_c = 100$ °C; (B), (C) and (D) Temperature evolution of the lattice dimensions *a*, *b* and *c*. The vertical dashed lines mark the temperatures at which changes in crystalline parameters are observed.

3.2. WAXS analysis as a function of temperature

The temperature-resolved WAXS patterns collected upon heating at 2 K/min after crystallization at $T_c = 100$ °C are presented in Fig. 2. Besides a few reflections due to the instrumental apparatus (marked in Fig. 2 with asterisks), the WAXS profiles display the main diffraction peaks located at $2\theta = 13.1, 14.6, 15.06, 17.3$ and $19.2°$, which correspond to (020), (021), (110), (-1,2,1) and (111) planes of PBS α-modification, respectively [39,40]. An increase in temperature produces small shifts in the position and variation of the intensity of the WAXS peaks, without the appearance of additional reflections. This indicates that only α-crystals are present in the PBS sample in the analyzed temperature range, without evidence of any other crystal modification, hence excluding any possible influence of crystal polymorphism on multiple melting behavior of PBS.

To investigate whether structural changes or reorganization phenomena occur upon heating, quantitative analysis of the *d*-spacings and areas of the most intense WAXS peaks was performed, together with an estimation of the lattice parameters evolution [53,54]. Data are presented in Fig. 3, where also the $c_{p,app}$ curve after crystallization at $T_c = 100$ °C is repeated in Fig. 3(A) to favor the comparison with the parameters derived from the WAXS analysis. (It is worth noting that the heat flow rate curve collected *in-line* with the WAXS/SAXS measurements, here not reported due to its considerable noise, was in perfect
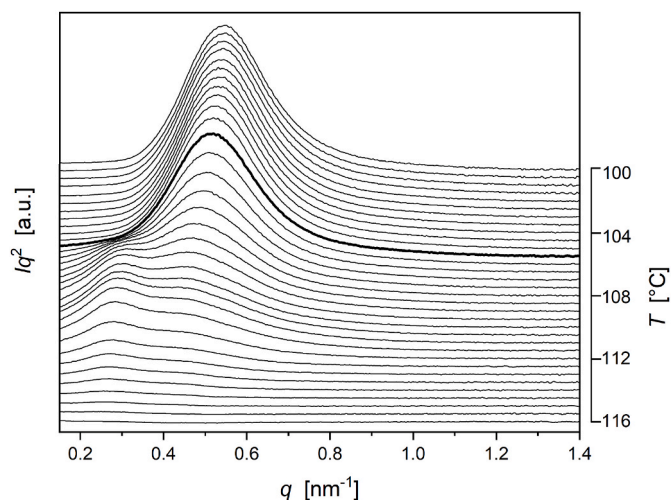
Fig. 5. Temperature-resolved Lorentz-corrected SAXS profiles of PBS upon heating (heating rate: 2 K/min) after isothermal crystallization at $T_c = 100\ °C$.

agreement with the curve displayed in Fig. 3(A)). The normalized areas of the (020) and (110) reflections are reported in Fig. 3(B) as a function of temperature. The intensity of both (020) and (110) peaks decreases upon heating in two different steps, with an intermediate temperature region in which the areas, and therefore the crystallinity, decrease more slowly, in agreement with the w_c evolution calculated from by the $c_{p,app}$ curve (Fig. 1(B)).

The temperature evolution of the inter-planar distances d_{110} and d_{020}, calculated from Bragg's law, are reported in Fig. 3(C) and (D), respectively. Both d_{110} and d_{020} do not display regular monotonic increase upon heating at 2 K/min, as expected from simple thermal lattice expansion. The d_{110} distance expands up to 105 °C, at which a change in the $c_{p,app}$ slope is observed (Fig. 3(A)), then it contracts, more distinctly in the temperature range 105–109 °C, and more slowly between 109 and 111 °C, with 109 °C corresponding to the peak temperature of the first major endotherm, and 111 °C the temperature at which the final endotherm begins. At higher temperatures, d_{110} becomes approximately constant.

The d_{020} inter-planar distance displays a different trend with the temperature increase, as it slightly increases up to 105 °C, then, instead of increasing due to thermal expansions, remains constant up to 109 °C. At higher temperatures, d_{020} increases again, more slowly in the temperature range 109–111 °C, and then more markedly above 111 °C. The non-monotonic d_{110} and d_{020} trends attest that a population of more stable crystals, characterized by the same crystal form, develops in the temperature range between 105 and 111 °C, in which decreasing or constant d_{110} and d_{020} spacings are observed, in place of the common continuous increase. This hypothesis is also confirmed by the temperature dependence of the lattice dimensions a, b and c, shown in Fig. 4 together with the repeated $c_{p,app}$ curve. The cell dimensions, calculated from the angular position of the five most intense peaks through a least-squares fitting procedure, do not increase regularly, as expected due to mere thermal expansion: after an initial increase, a and b remain approximately constant in the temperature range 105–109 °C, then increase slowly between 109 and 111 °C, before the final more marked enlargement, thus accrediting the growth of a crystal organization with denser packing.

The more stable crystal structure that develops in the temperature interval 105–111 °C must be characterized by a lower enthalpy content with respect to the original one, so that its formation might be revealed as an exotherm in the DSC plot. Unfortunately, this temperature range corresponds to the temperature region in which the first melting peak is located (Fig. 4(A)), so that the melting masks the simultaneous exothermic crystalline reorganization. The only trace of the final portion
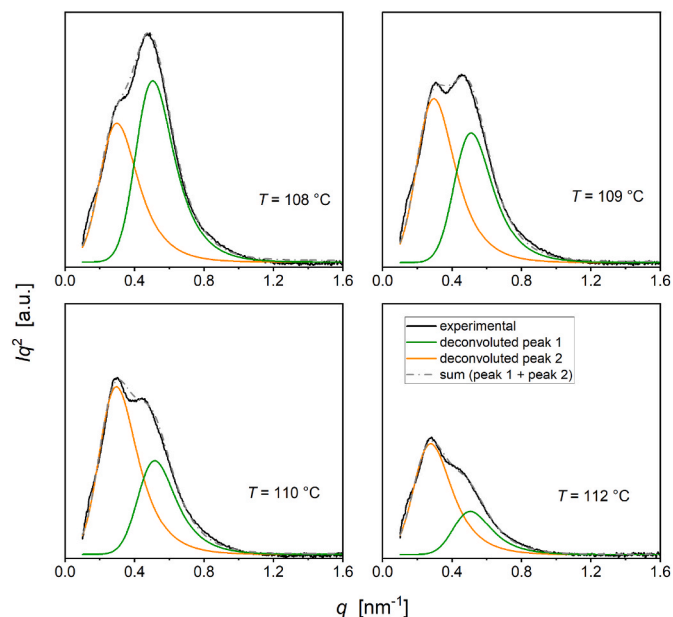

Fig. 6. Examples of multiple peakfit analysis of the Iq^2 profiles recorded at the indicated temperatures. The fit was obtained by using an exponentially modified Gaussian function.

of this exothermic process can be observed in the valley between the two melting peaks, where the $c_{p,app}$ value is lower than the $c_{p,app}$ at the beginning of the first peak. As the DSC signal always results from the algebraic sum of simultaneous endothermic and exothermic events, it follows that the fusion process in this temperature range must be inevitably more intense than the one that is observed.

### 3.3. SAXS analysis as a function of temperature

The Lorentz-corrected SAXS scans collected upon heating at 2 K/min after crystallization at $T_c = 100\ °C$, are shown in Fig. 5. Between 100 and 105 °C, the patterns display a well resolved single peak centered at $q = 0.54\ nm^{-1}$. Raising the temperature, the intensity of the peak decreases, and its position shifts towards smaller q values. Starting from about 105 °C, an additional peak appears at about $q = 0.30\ nm^{-1}$, and becomes well resolved at 108 °C. Importantly, the temperature at which the additional SAXS peak starts to develop corresponds to the temperature at which changes in the crystalline parameters are initially detected by WAXS analysis (Figs. 3–4).

Two separate SAXS peaks have sometimes been reported in case of the coexistence of two different morphological organizations [55–60]. For solution-crystallized polyethylene, the additional SAXS peak was ascribed to lamellar doubling occurring during annealing due to sliding motions in the solid state [55,56], whereas for poly [(R)-3-hydroxybutyrate)] single crystals, a simultaneous discontinuous increase in lamellar thickness was connected to partial melting and recrystallization mechanism [58].

The contribution of the two different crystalline populations to the overall Lorentz-corrected SAXS profiles was determined by means of a multiple peakfit program (commercial software OriginPro, OriginLab Corporation). Non-linear curve fitting was performed with an exponentially modified Gaussian function because this function was found appropriate to mathematically describe the single slightly asymmetric SAXS profiles at temperatures lower than 105 °C:

$$f(q) = y_o + \frac{A}{\tau} \exp\left[\frac{1}{2}\left(\frac{w}{\tau}\right)^2 - \frac{q - q_c}{\tau}\right] \int_{-\infty}^{z} \frac{1}{\sqrt{2\pi}} \exp\left(-\frac{y^2}{2}\right) dy \tag{5}$$
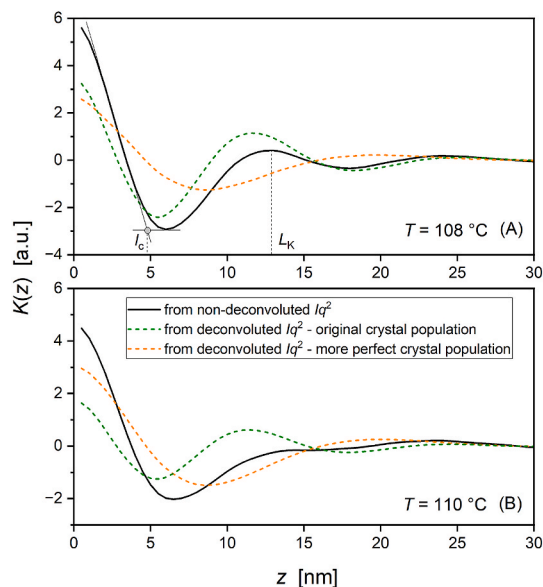
with $z = [(q-q_c)/w - w/\tau]$, where A is the peak area, τ the peak distortion,
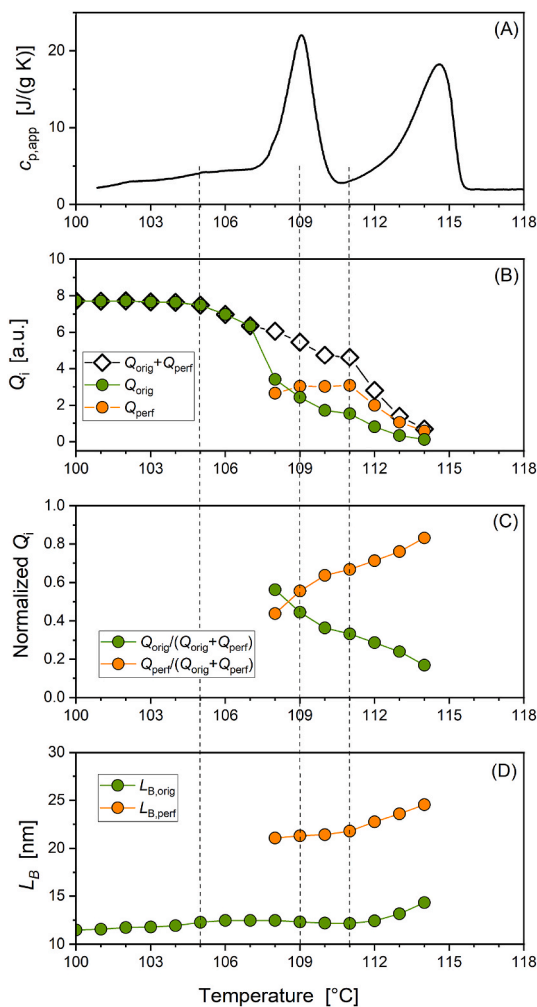
Fig. 7. (A) Apparent specific heat capacity ($c_{p,app}$) curve at 2 K/min after isothermal crystallization at $T_c = 100$ °C; (B) Temperature evolution of the invariants Q_{orig} and Q_{perf}, and their sum ($Q_{orig} + Q_{perf}$), calculated from the deconvoluted Lorentz-corrected SAXS profiles; (C) Normalized Q_{orig} and Q_{sec} as a function of temperature; (D) Bragg long periods (L_B) of the original and the more perfect crystal populations as a function of temperature. The vertical dashed lines mark the temperatures at which changes in crystalline parameters are observed.
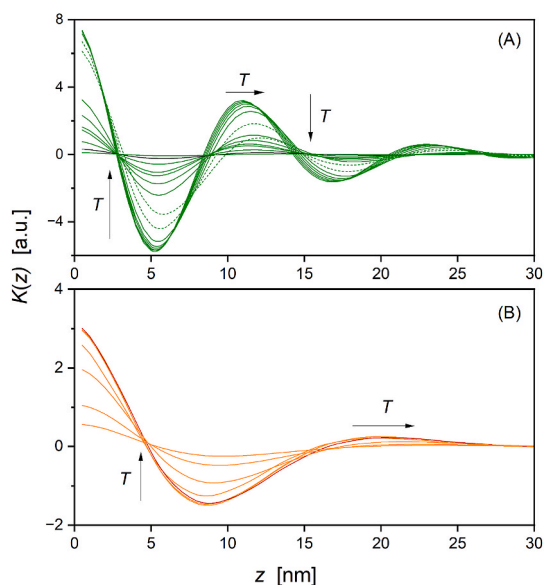

Fig. 8. Correlation functions $K(z)$ calculated from the non-deconvoluted Lorentz-corrected SAXS profiles (solid lines) and from the deconvoluted Lorentz-corrected SAXS profiles (dashed lines) at (A) $T = 108$ °C and (B) $T = 110$ °C. The thin black dashed and solid lines show how the long period L_K and the lamellar thickness l_c were estimated, respectively.

w the peak width and q_c the position of the peak maximum. Some examples of the deconvoluted Iq^2 curves are collected in Fig. 6. Confident peak fitting could be performed only starting from 108 °C, because the two Iq^2 peaks could be efficiently resolved only if present with comparable size.

Fig. 7 correlates the melting behaviour after crystallization at $T_c = 100$ °C (Fig. 7(A)) to quantitative information derived from the SAXS profiles. Fig. 7(B) displays the invariants Q_i calculated from the deconvoluted Lorentz-corrected SAXS profiles according to Eq. (1). The integration of Iq^2 was performed from the smallest experimental q value (0.10 nm^{-1}) to $q = 3.9$ nm^{-1}. Extrapolation of Iq^2 to $q = 0$ led to changes in the invariant values not higher than 0.3%. The invariant Q_i connected to the original Iq^2 peak centered at about $q = 0.54$ nm^{-1} (Q_{orig}) decreases mainly in correspondence of the first melting peak, in parallel with the new crystal organization growth, and then, at higher temperatures, more slowly. Conversely, the invariant Q_i linked to the Iq^2 peak centered at about $q = 0.30$ nm^{-1} (Q_{perf}) increases up to about 111 °C, *i.e.,* up to the end of the first major peak, and then decreases in parallel with the final melting peak. The formation of this new crystal population in the temperature range 105–111 °C is in agreement with the non-monotonic

changes exhibited by d_{110}, d_{200} and the lattice parameters (Figs. 3 and 4), all attesting to the growth of a more perfect crystal structure in this temperature range. About this connection, it has to be pointed out that the lattice parameters derived from the WAXS analysis are average values that account for both the crystal morphologies, the original and the more perfect ones, hence the structural parameters for the two separate crystal populations cannot be derived from WAXS data. The sum ($Q_{orig} + Q_{perf}$) decreases more slowly in the region between the first and second melting peaks, in agreement with the w_c trend. However, it has to be noted that the w_c and ($Q_{orig} + Q_{perf}$) trends are not perfectly coincident, as the scattering invariant is proportional to the product $[x_c(1-x_{c,l})]$, and also depends on the difference ($\rho_c - \rho_a$) (see Eq. (2)), which increases with temperature, due to the different thermal expansion of the crystalline and amorphous regions [44].

Additional information that can be derived from SAXS data, reported in Fig. 7(C), concerns the normalized Q_i values, defined as $Q_i/\Sigma Q_i$. In combination with Fig. 7(B), the normalized Q_{orig} and Q_{perf} data show that the population of the original crystals decreases in parallel with the increase of the recrystallized crystals. This further proves that the first melting peak in the $c_{p,app}$ curve has to be connected to the fusion of the original crystal population, only slightly reorganized/recrystallized due to the low heating rate. This is in agreement with the results of a recent study, which proved that the melting temperature of non-reorganized/non-recrystallized crystals PBS crystals grown at $T_c = 100$ °C is about 107 °C [24]. Conversely, the second peak has to be associated mainly to fusion of the more perfect crystal population. The fusion of the original population also extends up to about the end of the melting process, but its contribution to the second melting peak appears lower with respect to the more perfect crystals.

The long periods of the crystalline lamellae stacks for the original and the more stable crystal populations, calculated according to the Bragg law from the maxima of the Iq^2 deconvoluted profiles ($L_B = 2\pi/q_{max}$), are reported in Fig. 7(D). Besides an apparent $L_{B,orig}$ increase in the range 105–108 °C, which is a mere artefact due to the impossibility to deconvolute satisfactorily the experimental Iq^2 curves, Fig. 7(D) clearly shows the appearance of a double lamellar population. The long period of the crystal population that develops above 105 °C is approximately twice the long period of the original crystals, *i.e.,* 22 nm against

Fig. 9. Correlation functions $K(z)$ referring to: A) the original crystal population, from the non-deconvoluted Lorentz-corrected SAXS profiles calculated in the temperature range 100–107 °C, and from the deconvoluted Lorentz-corrected SAXS profiles in the temperature range 108–114 °C; (B) the more perfect crystal population, calculated from the deconvoluted Lorentz-corrected SAXS profiles. In the section (A) the dashed curves are the correlation functions at 106 and 107 °C.

12 nm. $L_{B,orig}$ increases only slightly between 100 and 111 °C, and more markedly above 112 °C. This behaviour suggests that the original crystal population substantially does not change its stack organization up to about 111 °C, in conjunction with the first melting peak. Conversely, the $L_{B,orig}$ increase that is observed above 112 °C has to be ascribed to reorganization of the original crystals [61,62], although the morphological parameters do not differ substantially from the initial ones. Also the $L_{B,perf}$ increase is not significant up to 111 °C, then it becomes more important in the temperature region of the final melting. This attests that both the crystalline populations undergo reorganization/recrystallization also in the region of the second melting peak, up to almost complete fusion.

Besides from the Bragg's law, the long period of crystalline lamellae stacks can be calculated also from the position of the first maximum of the correlation function $K(z)$ (L_K), whereas the average crystalline lamellar thickness (l_c) can be estimated from the linear tangent to the initial $K(z)$ decay, being the crystalline weight fraction lower than 0.5 [45–49]. Fig. 8 compares the correlation functions $K(z)$ calculated from the non-deconvoluted Lorentz-corrected SAXS profiles at 108 and 110 °C with the $K(z)$ curves derived from the deconvoluted Iq^2 curves. For $T = 108$ °C, the first maximum of the correlation functions calculated from the non-deconvoluted Lorentz-corrected SAXS profiles is clearly recognizable, but scarcely detectable for $T = 110$ °C. Fig. 8 displays that both the long period and the lamellar thickness derived from the non-deconvoluted Lorentz-corrected SAXS profiles are intermediate between the L_K and l_c values resulting from the deconvoluted Iq^2 curves.

All the correlation functions $K(z)$ calculated from the deconvoluted Lorentz-corrected SAXS profiles are collected in Fig. 9, with the section (A) referring to the original crystal population and the section (B) to the more perfect population. As regards the original crystal population, the correlation function was calculated from the non-deconvoluted Lorentz-corrected SAXS profiles in the temperature range 100–107 °C, and from the deconvoluted Lorentz-corrected SAXS profiles in the temperature range 108–114 °C. It is worth noting that the minima and the maxima of the $K(z)$ curves at 106 and 107 °C for the original crystal population, calculated from the non-deconvoluted Lorentz-corrected SAXS profiles
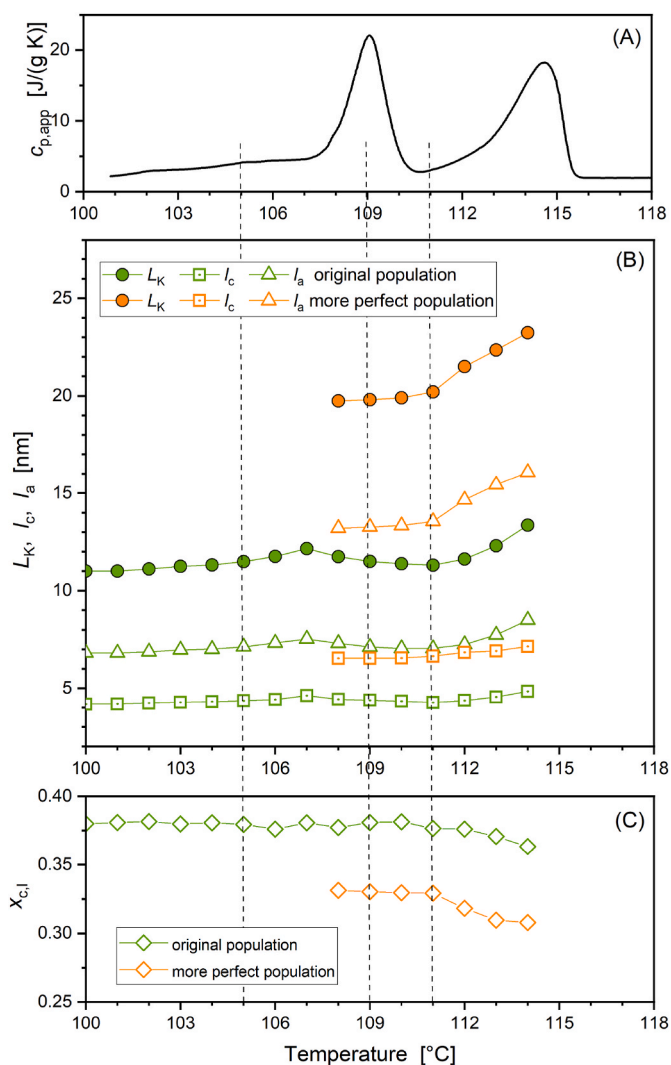

Fig. 10. (A) Apparent specific heat capacity ($c_{p,app}$) curve at 2 K/min after isothermal crystallization at $T_c = 100$ °C; (B) Temperature dependence of the long period (L_K), average lamellar crystal thickness (l_c), and average amorphous layer thickness (l_a) of the original and the more perfect crystal populations, calculated from the correlation functions; (C) temperature dependence of the linear crystallinity $x_{c,l}$ calculated for the original and more perfect crystal populations.

(dashed lines in Fig. 9(A)) appear slightly shifted to higher z values with respect to the trend of all the other curves, thus confirming that the more perfect crystal population is already present at 106 °C.

The long period (L_K) and the average lamellar thickness (l_c) of the original and the more perfect crystal populations, derived from the correlation functions, are displayed in Fig. 10 as a function of temperature, together with the average amorphous layer thickness (l_a) calculated by difference ($l_a = L_K - l_c$). As explained above, the L_K and l_c values in the temperature range 105–108 °C have to be considered constant. The L_K values are very close to the long periods calculated by the Bragg's law, being lower of only about 1 nm (see Fig. 7(D)), in agreement with previous reports [45,63]. The average lamellar thickness of the original crystals is about 4 nm at 100 °C. It increases slightly upon heating until it becomes about 5 nm at 114 °C. Very similar values have been reported in the literature [5,24]. The average lamellar thickness of the more perfect crystals is 6.5 nm at 108 °C, and about 7 nm at 114 °C. At 100 °C the average amorphous layer thickness of the original crystal population is about 7 nm, which becomes about 8.5 nm at 114 °C, whereas for the more perfect crystal population l_a is 13 nm, at 108 °C, and about 16 nm
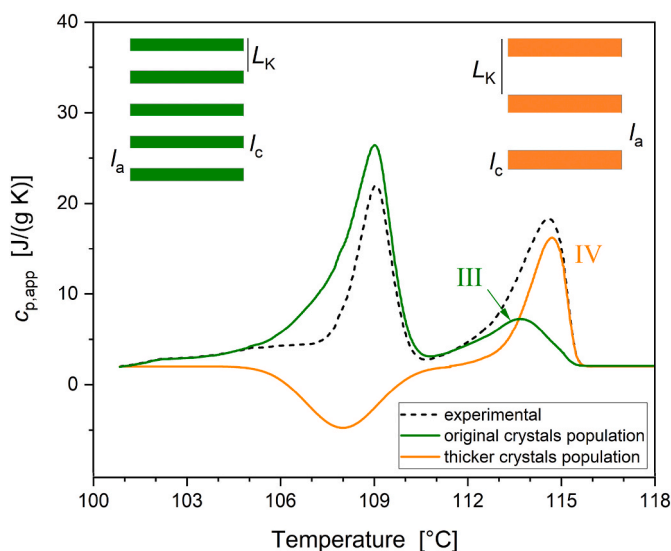
Fig. 11. Schematic description of the contribution of the different crystal populations to the experimental $c_{p,app}$ curve. In the Figure also a schematic one-dimensional representation of the lamellar stacks of original (green bars) and thicker crystals (orange bars) is displayed, with the bars representing lamellae (l_c = lamellar thickness, l_a = amorphous layer thickness, L_K = long period). (For interpretation of the references to color in this figure legend, the reader is referred to the Web version of this article.)

at 114 °C. The higher increase in l_a occurs in parallel with the second melting peak, in connection also with the higher thermal expansion of the amorphous regions at high temperatures [64].

Fig. 10(B) also displays the linear crystallinity ($x_{c,l}$) for the two different morphologies, which was quantified as $x_{c,l} = l_c/L_K$, as a function of temperature [46]. The linear crystallinity of the original crystals at 100 °C is about 0.38. This value is very close to the initial weight fraction crystallinity w_c, which could be transformed into volumetric bulk crystallinity (x_c) if the crystal and amorphous densities at 100 °C were known. By assuming the density values at room temperature (ρ_c = 1.33 g/cm^3 [40] and ρ_a = 1.26 g/cm^3 [65]), an initial x_c of 0.37 can be approximately assessed. This means that α_S, the volume fraction of the lamellar stacks within the total sample, which can be estimated as $\alpha_S = x_c/x_{c,l}$ [46], is close to 1. This high α_S value can be ascribable to the high PBS crystallizability [5,6,14,15,19]. The linear crystallinity for the original crystal population is higher than $x_{c,l}$ calculated for the more perfect morphology due to the lower difference (l_a - l_c). Both the linear crystallinities appear substantially constant with increasing temperature. This behavior, which has already been reported for other polymers, suggests that the lamellar stacks are not partially destroyed upon heating and melt entirely at the same time [66]. The slight decrease observed above 111 °C, in parallel with the second melting peak, for both the $x_{c,l}$ trends can be explained as an effect due to the higher thermal expansion of the amorphous regions at high temperatures.

A tentative schematic description of the contribution of the different crystal populations to the overall melting behavior is proposed in Fig. 11. By taking into account the Q values at 111 °C, *i.e.*, at the beginning of the second $c_{p,app}$ peak (see Fig. 7(B)), and the corresponding $x_{c,l}$ values (see Fig. 10(C)) for the two different crystal populations, and by assuming approximately identical the difference (ρ_c - ρ_a), the ratio between the volumetric bulk crystallinities of the thicker and the original crystal populations in the temperature region of the second melting peak has been calculated through Eq. (2). On the basis of this value, which is approximately 1.5, a peak with the appropriate area has been drawn in the highest temperature region and assigned to the fusion of the more perfect crystal population. In parallel, to reproduce the growth of this crystal population, an exothermic peak with identical area has been drawn between 105 and 111 °C, which are the

temperature limits for the formation of the thicker crystals, as attested by the WAXS and SAXS analyses (see Figs. 3 and 7). Thus, the difference between the experimental $c_{p,app}$ curve and the crystallization and melting curves relative to the second crystal morphology represents the fusion of the original crystal population. This fusion occurs in two steps, with the peak at higher temperatures, between 111 and 115 °C, associated to reorganized crystals characterized by slightly increased lamellar thickness (see Fig. 10). This interpretation is perfectly in line with the melting behavior of PBS after crystallization at lower T_cs (see Fig. 1), which displays two final endotherms (III and IV) that progressively overlap, merging into one. Thus, also after crystallization at T_c = 100 °C, the final portion of the melting comprises two different endotherms, which can be identified as peak III and peak IV, respectively.

The trend exhibited by endotherms III and IV at increasing T_c is, however different: the temperature at which endotherm III is centered increases with T_c, whereas endotherm IV is independent of T_c. This behavior suggests that two different reorganization mechanisms coexist upon heating, leading to different melting peaks. Endotherm III could be the fusion of the original crystals thickened upon heating due to solid-state lamellar thickening, a reorganization mechanism that has been proposed for PBS [67], in agreement with the significant molecular mobility of PBS crystals attested at high temperature [68]. Conversely, the T_c independence of the final endotherm suggests a marked change in crystal stability, which could take place through fusion and recrystallization, *i.e.*, melting of original crystals, with possible formation of a not completely relaxed melt and successive fast recrystallization into thicker crystals [69].

When crystallized from the quiescent melt, PBS forms big spherulites, with diameters larger than 100 μm for T_c higher than 70 °C [70–72], which suggests that the lateral dimensions of the original lamellae are large. The association between lamellar thickness (l_c) and melting temperature (T_m) can be quantified by means of the Gibbs-Thomson equation [73]:

$$T_m = T_m{}^\circ \left(1 - \frac{2\sigma_e}{l_c \Delta h_m{}^\circ} \right) \tag{6}$$

where $T_m{}^\circ$ is the equilibrium melting temperature, σ_e the fold surface free energy, and $\Delta h_m{}^\circ$ is the 100% crystalline enthalpy of melting. From the two melting peak temperatures of the original crystal population, T_{m1} = 109 °C and T_{m2} = 113.5 °C, (see Fig. 11) at which lamellar thicknesses of 4.3 and 4.7 nm were respectively estimated (see Fig. 10), by assuming $T_m{}^\circ$ = 135 °C [4,74] and $\Delta h_m{}^\circ$ = 2.6·10^8 J/m^3 [23], σ_e values of 3.5·10^{-2} and 3.2·10^{-2} J/m^2 can be derived. The first calculated σ_e value is in excellent agreement with σ_e data obtained from crystal growth kinetics at temperatures between 80 and 106 °C (σ_e = 3.4–3.6·10^{-2} J/m^2) [19,70]. This result confirms that the first melting peak can be confidently associated to the fusion of the original, only minimally reorganized crystals. Conversely, the slightly lower σ_e value connected to the second endotherm confirms that the melting event centered at 113.5 °C is associated to crystals slightly thickened at temperatures higher than T_c, as σ_e slightly decreases with increasing temperature [73]. By assuming large lateral dimensions also for the thicker crystal population, a σ_e value of 4.7·10^{-2} J/m^2 can be estimated by means of the Gibbs-Thomson equation, being T_m = 114.6 °C and l_c = 7.2 nm. This σ_e value is higher than the ones relative to the original crystal population. As σ_e is connected to the work necessary to fold the polymer chains to obtain the appropriate crystalline configuration [73], it is possible that higher energy and additional rearrangements are required to generate the new crystal population if recrystallization occurs from a not completely relaxed melt [69]. For the same reason, residual organized chain conformations could hinder the formation of regular and smooth surfaces and lead to fluctuations in the fold period, with consequent σ_e increase [73].

The thickness distribution of the PBS lamellae crystallized at 100 °C is narrow [24], thus it is challenging to visualize the specific positions
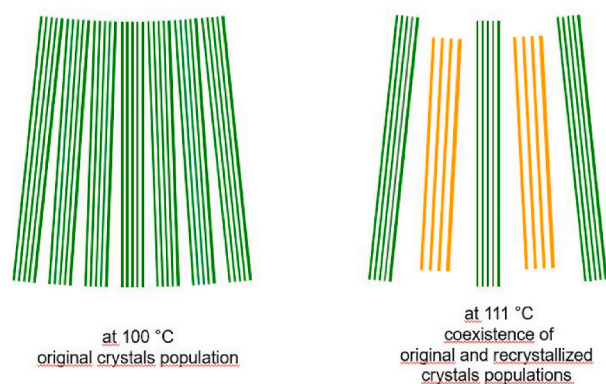
Fig. 12. Schematic representation of possible lamellae organization at 100 °C (left), with presence of only original crystals population (green lamellae), and at temperature around 111 °C (right), with presence of original and recrystallized crystals populations (green and orange lamellae, respectively). (For interpretation of the references to color in this figure legend, the reader is referred to the Web version of this article.)

hosting the recrystallized thicker lamellae. A possible organization of the two coexistent crystal populations around 111 °C, *i.e.*, between the low and high temperatures melting peaks, is sketched in Fig. 12, with the stacks of the thicker recrystallized crystals located between stacks of the original slightly thickened crystals.

4. Conclusions

The various thermal events occurring upon heating in semicrystalline PBS, which lead to multiple melting behavior, were clarified by temperature-dependent synchrotron WAXS/SAXS analysis. Combined temperature-dependent WAXS and SAXS measurements of PBS isothermally crystallized at 100 °C proved that, besides the original lamellae, an additional crystal population, characterized by markedly thicker lamellae, develops upon heating. Deconvolution of the double Lorentz-corrected SAXS profiles allowed to derive the temperature dependence of the lamellar thickness for the two different crystal populations. The lamellar thickness increase of the thicker crystal population is discontinuous with respect to the lamellar thickness trend exhibited by the original population.

The two endotherms that compose the melting behavior after crystallization at $T_c = 100$ °C were assigned to specific processes: the low temperature melting peak was connected to the fusion of minimally reorganized original crystals, whereas the higher temperature melting peak was proven to originate from overlapping of separate melting processes, connected to the two different crystalline populations. Different mechanisms that can produce the two crystal populations upon heating were hypothesized: (*i*) thickening at high temperature, presumably in the solid state, and (*ii*) fusion followed by recrystallization, with the formation of thicker lamellae. Fusion of these two different populations overlaps in the high temperature side of the overall melting process, resulting in a single wide final endotherm.

CRediT authorship contribution statement

Maria Cristina Righetti: Conceptualization, Data curation, Formal analysis, Investigation, Methodology, Supervision, Writing – original draft, Writing – review & editing. **Maria Laura Di Lorenzo:** Validation, Writing – original draft, Writing – review & editing. **Dario Cavallo:** Resources, Formal analysis, Validation, Writing – review & editing. **Alejandro J. Müller:** Methodology, Validation, Writing – review & editing. **Massimo Gazzano:** Data curation, Formal analysis, Writing – original draft, Writing – review & editing.

Declaration of competing interest

The authors declare that they have no known competing financial interests or personal relationships that could have appeared to influence the work reported in this paper.

Data availability

Data will be made available on request.

References

[1] G.-Q. Chen, M.K. Patel, Plastics derived from biological sources: present and future: a technical and environmental review, Chem. Rev. 112 (2012) 2082–2099, https://doi.org/10.1021/cr200162d.

[2] O. Platnieks, S. Gaidukovs, V.K. Thakur, A. Barkane, S. Beluns, Bio-based poly (butylene succinate): recent progress, challenges and future opportunities, Eur. Polym. J. 161 (2021), 110855, https://doi.org/10.1016/j.eurpolymj.2021.110855.

[3] M. Barletta, C. Aversa, M. Ayyoob, A. Gisario, K. Hamad, M. Mehrpouya, H. Vahabi, Poly(butylene succinate) (PBS): materials, processing, and industrial applications, Prog. Polym. Sci. 132 (2022), 101579, https://doi.org/10.1016/j.progpolymsci.2022.101579.

[4] T. Miyata, T. Masuko, Crystallization behaviour of poly(tetramethylene succinate), Polymer 39 (1998) 1399–1404, https://doi.org/10.1016/S0032-3861(97)00418-7.

[5] Z. Gan, H. Abe, H. Kurokawa, Y. Doi, Solid-state microstructures, thermal properties, and crystallization of biodegradable poly(butylene succinate) (PBS) and its copolyesters, Biomacromolecules 2 (2001) 605–613, https://doi.org/10.1021/bm015535e.

[6] J. Jiang, E. Zhuravlev, W.-B. Hu, C. Schick, D.-S. Zhou, The Effect of self-nucleation on isothermal crystallization kinetics of poly(butylene succinate) (PBS) investigated by differential fast scanning calorimetry, Chin. J. Polym. Sci. 35 (2017) 1009–1019, https://doi.org/10.1007/s10118-017-1942-5.

[7] J. Xu, B.-H. Guo, Poly(butylene succinate) and its copolymers: research, development and industrialization, Biotechnol. J. 5 (2010) 1149–1163, https://doi.org/10.1002/biot.201000136.

[8] M. Puchalski, G. Szparaga, T. Biela, A. Gutowska, S. Sztajnowski, I. Krucinska, Molecular and supramolecular changes in polybutylene succinate (PBS) and polybutylene succinate adipate (PBSA) copolymer during degradation in various environmental conditions, Polymers 10 (2018) 251, https://doi.org/10.3390/polym10030251.

[9] M.L.A. Jansen, W.M. van Gulik, Towards large scale fermentative production of succinic acid, Curr. Opin. Biotechnol. 30 (2014) 190–197, https://doi.org/10.1016/j.copbio.2014.07.003.

[10] H. Chung, J.E. Yang, J.Y. Ha, T.U. Chae, J.H. Shin, M. Gustavsson, S.Y. Lee, Bio-based production of monomers and polymers by metabolically engineered microorganisms, Curr. Opin. Biotechnol. 36 (2015) 73–84, https://doi.org/10.1016/j.copbio.2015.07.003.

[11] M. Gigli, M. Fabbri, N. Lotti, R. Gamberini, B. Rimini, A. Munari, Poly(butylene succinate)-based polyesters for biomedical applications: a review, Eur. Polym. J. 75 (2016) 431–460, https://doi.org/10.1016/j.eurpolymj.2016.01.016.

[12] S. Mallardo, V. De Vito, M. Malinconico, M.G. Volpe, G. Santagata, M.L. Di Lorenzo, Poly (butylene succinate)-based composites containing β-cyclodextrin/d-limonene inclusion complex, Eur. Polym. J. 79 (2016) 82–96, https://doi.org/10.1016/j.eurpolymj.2016.04.024.

[13] M.L. Di Lorenzo, Poly(l-Lactic acid)/poly(butylene succinate) biobased biodegradable blends, Polym. Rev. 61 (2021) 457–492, https://doi.org/10.1080/15583724.2020.1850475.

[14] D.G. Papageorgiou, E. Zhuravlev, G.Z. Papageorgiou, D. Bikiaris, K. Chrissafis, C. Schick, Kinetics of nucleation and crystallization in poly(butylene succinate) nanocomposites, Polymer 55 (2014) 6725–6734, https://doi.org/10.1016/j.polymer.2014.11.014.

[15] M.L. Di Lorenzo, R. Androsch, M.C. Righetti, Low-temperature crystallization of poly (butylene succinate), Eur. Polym. J. 94 (2017) 384–391, https://doi.org/10.1016/j.eurpolymj.2017.07.025.

[16] E.S. Yoo, S.S. Im, Melting behavior of poly(butylene succinate) during heating scan by DSC, J. Polym. Sci., Polym. Phys. 37 (1999) 1357–1366, https://doi.org/10.1002/(SICI)1099-0488(19990701)37:13<1357::AID-POLB2>3.0.CO;2-Q.

[17] M. Yasuniwa, T. Satou, Multiple melting behavior of poly(butylene succinate). I. Thermal analysis of melt-crystallized samples, J. Polym. Sci., Polym. Phys. 40 (2002) 2411–2420, https://doi.org/10.1002/polb.10298.

[18] Z. Qiu, M. Komura, T. Ikehara, T. Nishi, DSC and TMDSC study of melting behaviour of poly(butylene succinate) and poly(ethylene succinate), Polymer 44 (2003) 7781–7785, https://doi.org/10.1016/j.polymer.2003.10.045.

[19] G.Z. Papageorgiou, D.N. Bikiaris, Crystallization and melting behavior of three biodegradable poly(alkylene succinates). A comparative study, Polymer 46 (2005) 12081–12092, https://doi.org/10.1016/j.polymer.2005.10.073.

[20] M. Yasuniwa, S. Tsubakihara, T. Satou, K. Iura, Multiple melting behavior of poly (butylene succinate). II. Thermal analysis of isothermal crystallization and melting process, J. Polym. Sci., Polym. Phys. 43 (2005) 2039–2047, https://doi.org/10.1002/polb.20499.

[21] X. Wang, J. Zhou, L. Li, Multiple melting behavior of poly(butylene succinate), Eur. Polym. J. 43 (2007) 3163–3170, https://doi.org/10.1016/j.eurpolymj.2007.05.013.

[22] F. Signori, M. Pelagaggi, S. Bronco, M.C. Righetti, Amorphous/crystal and polymer/filler interphases in biocomposites from poly(butylene succinate), Thermochim. Acta 543 (2012) 74–81, https://doi.org/10.1016/j.tca.2012.05.006.

[23] M.C. Righetti, M.L. Di Lorenzo, P. Cinelli, M. Gazzano, Temperature dependence of the rigid amorphous fraction of poly(butylene succinate), RSC Adv. 11 (2021), 25731, https://doi.org/10.1039/D1RA03775G.

[24] C. Schick, A. Toda, R. Androsch, The narrow thickness distribution of lamellae of poly(butylene succinate) formed at low melt supercooling, Macromolecules 54 (2021) 3366–3376, https://doi.org/10.1021/acs.macromol.1c00388.

[25] R. Zhang, K. Jariyavidyanont, E. Zhuravlev, C. Schick, R. Androsch, Zero-entropy-Production melting temperature of crystals of poly(butylene succinate) formed at high supercooling of the melt, Macromolecules 55 (2022) 965–970, https://doi.org/10.1021/acs.macromol.1c02394.

[26] P. Pan, Y. Inoue, Polymorphism and isomorphism in biodegradable polyesters, Prog. Polym. Sci. 34 (2009) 605–640, https://doi.org/10.1016/j.progpolymsci.2009.01.003.

[27] J.S. Chung, P. Cebe, Melting behaviour of poly(phenylene sulphide): 1. Single-stage melt crystallization, Polymer 33 (1992) 2312–2324, https://doi.org/10.1016/0032-3861(92)90522-X.

[28] H. Marand, A. Alizadeh, R. Farmer, R. Desai, V. Velikov, Influence of structural and topological constraints on the crystallization and melting behavior of polymers. 2. Poly(arylene ether ether ketone), Macromolecules 33 (2000) 3392–3403, https://doi.org/10.1021/ma9913562.

[29] Y. Furushima, M. Nakada, K. Ishikiriyama, A. Toda, R. Androsch, E. Zhuravlev, C. Schick, Two crystal populations with different melting/reorganization kinetics of isothermally crystallized polyamide 6, J. Polym. Sci., Polym. Phys. 54 (2016) 2126–2138, https://doi.org/10.1002/polb.24123.

[30] L. Sangroniz, B. Wang, Y. Su, G. Liu, D. Cavallo, D. Wang, A.J. Müller, Fractionated crystallization in semicrystalline polymers, Prog. Polym. Sci. 115 (2021) 101376, https://doi.org/10.1016/j.progpolymsci.2021.101376.

[31] M.C. Righetti, M. Laus, The biphasic behaviour of a thermotropic polymesomorphic polyester I. Time evolution of phase separation, Polymer 41 (2000) 8355–8362, https://doi.org/10.1016/S0032-3861(00)00249-4.

[32] M.C. Righetti, A. Boggioni, M. Laus, D. Antonioli, K. Sparnacci, L. Boarino, Thermal and mechanical properties of PES/PTFE composites and nanocomposites, J. Appl. Polym. Sci. 130 (2013) 3624–3633, https://doi.org/10.1002/app.39613.

[33] G. Capaccio, I. Ward, Preparation of ultra-high modulus linear polyethylenes; effect of molecular weight and molecular weight distribution on drawing behaviour and mechanical properties, Polymer 15 (1974) 233–238, https://doi.org/10.1016/0032-3861(74)90038-X.

[34] H. Xu, B.S. Ince, P. Cebe, Development of the crystallinity and rigid amorphous fraction in cold-crystallized isotacticpolystyrene, J. Polym. Sci., Polym. Phys. 41 (2003) 3026–3036, https://doi.org/10.1002/polb.10625.

[35] M.C. Righetti, M.L. Di Lorenzo, E. Tombari, M. Angiuli, The low-temperature endotherm in poly(ethylene terephthalate): partial melting and rigid amorphous fraction mobilization, J. Phys. Chem. B 112 (14) (2008) 4233–4241, https://doi.org/10.1021/jp076399w.

[36] M.L. Di Lorenzo, M. Gazzano, M.C. Righetti, The role of the rigid amorphous fraction on cold crystallization of poly(3-hydroxybutyrate), Macromolecules 45 (2012) 5684–5691, https://doi.org/10.1021/ma3010907.

[37] A.A. Minakov, D.A. Mordvintsev, C. Schick, Melting and reorganization of poly (ethylene terephthalate) on fast heating (1000K/s), Polymer 45 (2004) 3755–3763, https://doi.org/10.1016/j.polymer.2004.03.072.

[38] A.A. Minakov, D.A. Mordvintsev, R. Tol, C. Schick, Melting and reorganization of the crystalline fraction and relaxation of the rigid amorphous fraction of isotactic polystyrene on fast heating (30,000 K/min), Thermochim. Acta 442 (2006) 25–30, https://doi.org/10.1016/j.tca.2005.11.032.

[39] K.J. Ihn, E.S. Yoo, S.S. Im, Structure and morphology of poly(tetramethylene succinate) crystals, Macromolecules 28 (1995) 2460–2464, https://doi.org/10.1021/ma00111a045.

[40] Y. Ichikawa, H. Kondo, Y. Igarashi, K. Noguchi, K. Okuyama, J. Washiyama, Crystal structures of α and β forms of poly(tetramethylene succinate), Polymer 41 (2000) 4719–4727, https://doi.org/10.1016/S0032-3861(99)00659-X.

[41] Y. Ichikawa, J. Suzuki, J. Washiyama, Y. Moteki, K. Noguchi, K. Okuyama, Strain-induced crystal modification in poly(tetramethylene succinate), Polymer 35 (1994) 3338–3339, https://doi.org/10.1016/0032-3861(94)90144-9.

[42] S.M. Sarge, W. Hemminger, E. Gmelin, G.W.H. Höhne, H.K. Cammenga, W. Eysel, Metrologically based procedures for the temperature, heat and heat flow rate calibration of DSC, J. Therm. Anal. 49 (1997) 1125–1134, https://doi.org/10.1007/BF01996802.

[43] V. Dyadkin, P. Pattison, V. Dmitriev, D. Chernyshov, A new multipurpose diffractometer PILATUS@SNBL, J. Synchtrotron Radiat. 23 (2016) 825–829, https://doi.org/10.1107/S1600577516002411.

[44] K.-N. Krüger, H.G. Zachman, Investigation of the melting behavior of poly(aryl ether ketones) by simultaneous measurements of SAXS and WAXS employing synchrotron radiation, Macromolecules 26 (1993) 5202–5208, https://doi.org/10.1021/ma00071a035.

[45] R. Verma, H. Marand, B. Hsiao, Morphological changes during secondary crystallization and subsequent melting in poly(ether ether keton) as studied by real time small angle X-ray scattering, Macromolecules 29 (1996) 7767–7775, https://doi.org/10.1021/ma951727o.

[46] A.M. Jonas, T.P. Russel, D.Y. Yoon, Synchrotron X-ray scattering studies of crystallization of poly(ether-ether-ketone) from the glass and structural changes during subsequent heating-cooling processes, Macromolecules 28 (1995) 8491–8503, https://doi.org/10.1021/ma00129a005.

[47] G.R. Strobl, M. Schneider, Direct evaluation of the electron density correlation function of partially crystalline polymers, J. Polym. Sci., Polym. Phys. 18 (1980) 1343–1359, https://doi.org/10.1002/pol.1980.180180614.

[48] B. Goderis, H. Reynaers, M.H.J. Koch, V.B.F. Mathot, Use of SAXS and linear correlation functions for the determination of the crystallinity and morphology of semi-crystalline polymers. Application to linear polyethylene, J. Polym. Sci., Polym. Phys. 37 (1999) 1715–1738, https://doi.org/10.1002/(SICI)1099-0488(19990715)37:14<1715::AID-POLB15>3.0.CO;2-F.

[49] B.S. Hsiao, R.K. Verma, A novel approach to extract morphological variables in crystalline polymers from time-resolved synchrotron SAXS data, J. Synchrotron Radiat. 5 (1998) 23–29, https://doi.org/10.1107/S0909049597010091.

[50] Y. Kong, J.N. Hay, Multiple melting behaviour of poly(ethylene terephthalate), Polymer 44 (2003) 623–633, https://doi.org/10.1016/S0032-3861(02)00814-5.

[51] B.B. Sauer, W.G. Kampert, E. Neal Blanchard, S.A. Threefoot, B.S. Hsiao, Temperature modulated DSC studies of melting and recrystallization in polymers exhibiting multiple endotherms, Polymer 41 (2000) 1099–1108, https://doi.org/10.1016/S0032-3861(99)00258-X.

[52] M.C. Righetti, M. Laus, M.L. Di Lorenzo, Temperature dependence of the rigid amorphous fraction in poly(ethylene terephthalate), Eur. Polym. J. 58 (2014) 60–68, https://doi.org/10.1016/j.eurpolymj.2014.06.005.

[53] J. Zhang, K. Tashiro, H. Tsuji, A.J. Domb, Disorder-to-Order phase transition and multiple melting behavior of poly(l-lactide) investigated by simultaneous measurements of WAXS and DSC, Macromolecules 41 (2008) 1352–1357, https://doi.org/10.1021/ma0706071.

[54] A.P. Melnikov, M. Rosenthal, D.A. Ivanov, What thermal analysis can tell us about melting of semicrystalline polymers: exploring the general validity of the technique, ACS Macro Lett. 7 (2018) 1426–1431, https://doi.org/10.1021/acsmacrolett.8b00754.

[55] S. Rastogi, A.B. Spoelstra, J.G.P. Goossens, P.J. Lemstra, Chain mobility in polymer systems: on the borderline between solid and melt. 1. Lamellar doubling during annealing of polyethylene, Macromolecules 30 (1997) 7880–7889, https://doi.org/10.1021/ma970519o.

[56] H. Matsuda, T. Aoike, H. Uehara, T. Yamanobe, T. Komoto, Overlapping of different rearrangement mechanisms upon annealing for solution-crystallized polyethylene, Polymer 42 (2001) 5013–5021, https://doi.org/10.1016/S0032-3861(00)00893-4.

[57] H. Hama, K. Tashiro, Structural changes in isothermal crystallization process of polyoxymethylene investigated by time-resolved FTIR, SAXS and WAXS measurements, Polymer 44 (2003) 6973–6988, https://doi.org/10.1016/j.polymer.2003.08.019.

[58] T. Sawayanagi, T. Tanaka, T. Iwata, H. Abe, Y. Doi, K. Ito, T. Fujisawa, M. Fujita, Real-time synchrotron SAXS and WAXD studies on annealing behavior of poly[(R)-3-hydroxybutyrate] single crystals, Macromolecules 39 (2006) 2201–2208, https://doi.org/10.1021/ma052425h.

[59] C. Marega, V. Causin, A. Marigo, The morphology, structure and melting behaviour of cold crystallized isotactic polystyrene, Macromol. Res. 14 (2006) 588–595, https://doi.org/10.1007/BF03218729.

[60] H. Zhu, Y. Lv, T. Duan, M. Zhu, Y. Li, W. Miao, Z. Wang, In-situ investigation of multiple endothermic peaks in isomorphous poly(3-hydroxybutyrate-co-3-hydroxyvalerate) with low HV content by synchrotron radiation, Polymer 169 (2019) 1–10, https://doi.org/10.1016/j.polymer.2019.01.077.

[61] Z.-G. Wang, B.S. Hsiao, B.B. Sauer, W.G. Kampert, The nature of secondary crystallization in poly(ethylene terephthalate), Polymer 40 (1999) 4615–4627, https://doi.org/10.1016/S0032-3861(99)00067-1.

[62] K. Heo, J. Yoon, K.S. Jin, S. Jin, H. Sato, Y. Ozaki, M.M. Satkowski, I. Noda, M. Ree, Structural evolution in microbial polyesters, J. Phys. Chem. B 112 (2008) 4571–4582, https://doi.org/10.1021/jp711136x.

[63] B.S. Hsiao, K.C.H. Gardner, D.Q. Wu, B. Chu, Time-resolved X-ray study of poly (aryl ether ether ketone) crystallization and melting behavior: 1. Crystallization, Polymer 34 (1993) 3986–3995, https://doi.org/10.1016/0032-3861(93)90658-W.

[64] B. Lee, T.J. Shin, S.W. Lee, J. Yoon, J. Kim, M. Ree, Secondary crystallization behavior of poly(ethylene isophthalate-co-terephthalate): time-resolved small-angle X-ray scattering and calorimetry studies, Macromolecules 37 (2004) 4174–4184, https://doi.org/10.1021/ma0357321.

[65] D.W. Van Krevelen, K. te Nijenhuis, Properties of Polymers, fourth ed., Elsevier, Amsterdam, 2009.

[66] Z.-G. Wang, B.S. Hsiao, B.X. Fu, L. Liu, F. Yeh, B.B. Sauer, H. Chang, J.M. Schultz, Correct determination of crystal lamellar thickness in semicrystalline poly(ethylene terephthalate) by small-angle X-ray scattering, Polymer 41 (2000) 1791–1797, https://doi.org/10.1016/S0032-3861(99)00327-4.

[67] J. Duan, D. Guo, Annealing behavior of the novel morphology of poly(butylene succinate) lath-shaped single crystals, J. Polym. Sci., Polym. Phys. 47 (2009) 1492–1496, https://doi.org/10.1002/polb.21750.

[68] K. Kuwabara, Z. Gan, T. Nakamura, H. Abe, Y. Doi, Temperature dependence of the molecular motion in the crystalline region of biodegradable poly(butylene adipate), poly(ethylene succinate), and poly(butylene succinate), Polym. Degrad. Stabil. 84 (2004) 105–114, https://doi.org/10.1016/j.polymdegradstab.2003.09.017.

[69] K. Jariyavidyanont, R. Androsch, C. Schick, Crystal reorganization of poly (butylene terephthalate), Polymer 124 (2017) 274–283, https://doi.org/10.1016/j.polymer.2017.07.076.

[70] Z. Qiu, W. Yang, Crystallization kinetics and morphology of poly(butylene succinate)/poly(vinyl phenol) blend, Polymer 47 (2006) 6429–6437, https://doi.org/10.1016/j.polymer.2006.07.001.

[71] T. Wang, H. Wang, H. Li, Z.X. Gan, S. Yan, Banded spherulitic structures of poly (ethylene adipate), poly(butylene succinate) and in their blends, Phys. Chem. Chem. Phys. 11 (2009) 1619–1627, https://doi.org/10.1039/B817597G.

[72] Y. Zheng, G. Tian, J. Xue, J. Zhou, H. Huo, L. Li, Effects of isomorphic poly (butylene succinate-co-butylene fumarate) on the nucleation of poly(butylene succinate) and the formation of poly(butylene succinate) ring-banded spherulites, CrystEngComm 20 (2018) 1573–1587, https://doi.org/10.1039/C7CE02124K.

[73] J.D. Hoffman, G.T. Davis Jr., J.I. Lauritzen, The rate of crystallization of linear polymers with chain folding, in: N.B. Hannay (Ed.), Treatise on Solid State Chemistry Volume. 3 Crystalline and Noncrystalline Solids, Plenum Press, New York, 1976, pp. 497–614.

[74] Z. Qiu, M. Komura, T. Ikehara, T. Nishi, Poly(butylene succinate)/poly(vinyl phenol) blends. Part 1. Miscibility and crystallization, Polymer 44 (2003) 8111–8117, https://doi.org/10.1016/j.polymer.2003.10.030.